Corrosion Science 233 (2024) 112115

Contents lists available at ScienceDirect

Corrosion Science

journal homepage: www.elsevier.com/locate/corsci

Corrosion of austenitic and ferritic steels, Kovar, and molybdenum in liquid Sb-Bi alloys with different compositions

Renate Fetzer *, Annette Heinzel, Tianru Zhang, Alfons Weisenburger, Georg Müller

Institute for Pulsed Power and Microwave Technology (IHM), Karlsruhe Institute of Technology (KIT), Hermann-von-Helmholtz-Platz 1, Eggenstein-Leopoldshafen 76344, Germany

ARTICLE INFO

Keywords:
Corrosion
Austenitic steel
Ferritic steel
Kovar
Molybdenum
Liquid Sb-Bi alloy

ABSTRACT

Sb-Bi alloys may be applied as positive electrode in liquid metal batteries. In this work, the material compatibility of two steels (SS 316L and T91), Kovar 4J29, and molybdenum with $SbBi_9$, Sb_2Bi_8, and Sb_3Bi_7 is investigated in static corrosion tests for 740 h at around 450 °C. Kovar shows severe dissolution attack (800 µm depth for $SbBi_9$), which is mitigated at higher Sb contents due to the formation of Fe-Sb compounds. Both steels exhibit moderate corrosion depths (10–20 µm) for all Sb-Bi alloys thanks to the additional formation of stable Fe-Cr-Sb compounds. Good corrosion resistance is obtained for molybdenum.

1. Introduction

Liquid metal batteries are intensely researched in recent years due to their potential for large-scale electrical energy storage [1–4]. LMB cells consist of a liquid metal negative electrode, a molten salt electrolyte, and a liquid metal positive electrode, which self-segregate due to density differences and mutual immiscibility. All-liquid systems provide fast kinetics at the electrode-electrolyte interfaces enabling operation at high current densities, low maintenance costs, and cycling without any structural changes or degradation of the electrodes, which permits a long service life.

Heavily researched are LMBs with liquid lithium (Li) serving as negative electrode [2,5–9]. Lithium shows excellent electrochemical performance due to its high energy density, low melting point, and low solubility in the respective halide salt. Li may be combined with various positive electrode materials, but antimony (Sb) and Sb-containing alloys are favored due to its low cost and high cell voltage. The main disadvantage of antimony is its high melting point, why it is typically alloyed with another metal to reduce the melting point of the positive electrode. To avoid the environmental issues related with lead, alloying with tin (Sn) is considered as feasible option [6]. However, Sn does not contribute to the electrochemical reaction and thus lowers the energy density of the LMB cell. In addition, Sb-Sn alloys are very aggressive towards structural materials respectively positive current collector materials [10–13], which may significantly reduce the service life of the battery. Recently, bismuth (Bi) was researched as an alternative positive electrode material [7] or as an alloying element for Sb to form Sb-Bi [8] or Sb-Bi-Sn [9]. Bi participates in the lithiation/delithiation process and was even attributed self-healing effects. Additionally, Sb-Bi alloys not only perform well in Li-based LMB but also when combined with sodium as negative electrode [14,15]. Sodium is researched as alternative option to Li because of its economic and environmental advantages due to its high abundance in the earth crust.

Although Sb-Bi is expected to be less aggressive towards PCC materials than Sb-Sn, little is known about the corrosion behavior of metallic materials in contact with liquid Sb-Bi alloys. Generally, corrosion of solid materials in liquid metals is mainly driven by the solubility of the material's constituents in the liquid metal and the formation of intermediate compounds and/or solid solutions with the liquid metal at the interface between solid and liquid metal. In addition, impurities in the liquid metal such as oxygen and carbon may have a strong influence on the corrosion behavior.

Regarding the material compatibility with pure liquid Bi, ferritic iron, low-carbon steels, and low-alloy steels have good corrosion resistance against bismuth up to their transformation temperatures (about 700 °C), while nickel-containing austenitic stainless steels and high-nickel alloys have poor resistance to attack by bismuth [16,17]. This difference is caused by the high solubility of Ni in liquid Bi (7 mol% at 400 °C) in contrast to the low solubilities of Fe and Cr (8e-4 and 4e-3 mol %, respectively, at 400 °C). Similarly, molybdenum (Mo) has a very low solubility in liquid Bi and shows good resistance against dissolution attack by bismuth at temperatures up to 1010 °C [16–18]. A common

---

* Corresponding author.
E-mail address: renate.fetzer@kit.edu (R. Fetzer).

https://doi.org/10.1016/j.corsci.2024.112115
Received 19 February 2024; Received in revised form 30 April 2024; Accepted 3 May 2024

corrosion mitigation strategy against dissolution attack of, e.g., Ni-containing steels is to add a specific amount of oxygen to the liquid metal to in-situ grow a protective oxide layer on the material surface that impedes the dissolution of the alloying elements into the liquid metal and the penetration of the liquid metal into the solid material [19]. This mitigation strategy, however, does not work in environments such as liquid metal batteries that do not allow the use of oxygen. If solid materials are covered by a pre-formed oxide layer prior to exposure, such a layer will decompose due to the presence of stronger oxide formers in the system (e.g., Li) that catch all available oxygen. Besides, the oxygen impurity introduced by pre-formed oxide layers is detrimental to the performance of LMB cells.

Regarding pure antimony, corrosion data of course exist only for temperatures above its melting point (630 °C). For instance, Armco iron, cast iron, low-carbon steel, and cast steel have poor corrosion resistance to liquid Sb due to the formation of Fe-Sb compounds [16,17,20]. At 450 °C or 500 °C, feasible working temperatures of liquid Sb-Bi alloys, Sb can form stable intermediate compounds with Fe, Cr, Ni, and Co. On the other hand, the kinetics of their formation is expected to be reduced compared with the exposures to pure Sb at temperatures above 630 °C. Furthermore, it is unclear how the competing processes of dissolution (due to the presence of Bi) and formation of intermediate compounds (with Sb) interact with each other when considering the corrosion behavior in Sb-Bi alloys. Similar to an oxide scale, a compact solid layer composed of intermediate compounds and solid solutions may form during exposure at the sample surface and protect the material from dissolution corrosion or at least mitigate the dissolution process.

To the best of our knowledge, no study of corrosion in liquid Sb-Bi alloys can be found in literature. However, the corrosion behavior in other Sb-containing alloys such as Sb-Pb, Sb-Sn, or Sb-Bi-Sn was investigated. Static exposure to Sb_3Pb_7 at 450 °C for 500 h lead to an Fe-Sb corrosion layer ($FeSb_2$), $\sim$100 μm thick, on low-carbon steel and to an Fe-Cr-Ni-Sb, respectively Fe-Cr-Sb, corrosion layer of $\sim$10 μm thickness on the stainless steels 301 and 430 [21]. It was concluded that in case of SS 430 the Fe-Cr-Sb corrosion layer mitigated dissolution and material recession. Since the solubility of Fe and Cr is much lower in Pb than in Bi, these results cannot be directly transferred to Sb-Bi alloys. In another study [22], after 500 h static exposure at 500 °C to Sb-Bi-Sn alloys, a distinct Fe-Cr-Sb layer was observed at the surface of austenitic stainless steel 304, which was also proposed to mitigate the dissolution of Fe. The thickness of the Fe-Cr-Sb corrosion layer was 16 μm for $Sb_{50}Bi_{20}Sn_{30}$ and 32 μm for $Sb_{45}Bi_{45}Sn_{10}$. These results also can only give an indication but cannot predict the corrosion behavior in Sb-Bi alloys. However, they demonstrate the relevance of the alloy composition due to the competing actions of Sb and Bi in the corrosion process.

Therefore, in the present work, the corrosion behavior of various PCC candidate materials is investigated in liquid Sb-Bi alloys with three different compositions, namely Sb_3Bi_7, Sb_2Bi_8, and $SbBi_9$. By comparing the results of the exposure tests, the influence of the individual alloy components (Sb or Bi) on the corrosion behavior of the selected materials is specified. Regarding the test materials, two different steels (austenitic SS 316L and f/m steel T91), Kovar alloy, and molybdenum are selected. Stainless steel 316L is a commonly used structural material. However, it contains a rather high amount of Ni, which may have a detrimental effect due to its high solubility in Bi. Therefore, also the Fe-Cr steel T91 is investigated for comparison. The selection of the Fe-Co-Ni alloy Kovar 4J29 is motivated by the design of an LMB cell and its advantages for sealing. Finally, Mo is chosen as the most promising material because of its low solubility in Bi and the fact that is does not form intermediate phases with Sb. The materials and oxygen-poor conditions are motivated by the potential application as positive current collector in LMBs. However, the static corrosion study makes the results application-independent and valuable for all fields of liquid metal technology where corrosion cannot be mitigated by active oxygen control.

2. Materials and methods

2.1. Materials

The test materials in this work were 316L austenitic stainless steel (SS 316L) from two different sources (EUROTRANS-DEMETRA [23] and from stock, KIT), T91 ferritic-martensitic steel (EUROTRANS-DEMETRA [23]), 4J29 Kovar alloy (Dongguan Saijing special alloy Co. Ltd.), and molybdenum (Mo) metal (Plansee SE). The compositions of the steels and Kovar are listed in Table 1, where SS 316L from the two different batches are denoted as A (EUROTRANS-DEMETRA) and B and deviate mainly in their Ni content. Specimens from SS 316L-A were exposed to $SbBi_9$, while specimens from SS 316L-B were used for the corrosion tests in Sb_2Bi_8 and Sb_3Bi_7. All materials were cut into specimens of appropriate size (max. 30 ×8×2 mm) and ground by sandpaper with a grit size of 800 and 1200, successively, prior to exposure.

Sb and Bi were delivered by Haines & Maassen Metallhandelsgesellschaft GmbH. The Sb granular had a purity of 99.65 % and a granular size of 1–10 mm; the Bi possessed a purity of 99.99 % and a granular size of 1–3 mm. Because of a slightly oxidized surface of Bi, it was first melted in a stainless-steel crucible and the slag layer on top was removed. Then, the desired amount of molten Bi was poured into Al_2O_3-crucibles and cooled down to room temperature. Afterwards, the desired amount of granular Sb was added. Alloying of Sb and Bi took place under controlled Ar5%H_2 atmosphere at 700 °C, see below. The Sb-Bi alloys contained a small impurity ($<$0.1 %) from arsenic (As), which is known to be a very typical impurity of Sb and, thus, most probably stemmed from the Sb raw material.

2.2. Exposure tests

The pre-conditioning of the Sb-Bi alloys and the corrosion tests were performed in the COSTA facility, which consists of tubular furnaces with quartz tubes as reaction chambers [24]. The gas atmosphere in the quartz tubes is controlled by a gas control system including flow meters and oxygen sensors. For the present experiments, a continuous flow (100 mL/min) of Ar5%H_2 (mixture of argon and 5 vol% hydrogen, each with purity 6.0) was used, which resulted in an oxygen partial pressure $<10^{-34}$ bar at the test section. For melting and pre-conditioning of the Sb-Bi alloys, the alumina crucibles filled with about 100 g of Sb-Bi were placed inside the quartz tubes and exposed to the continuous Ar5%H_2 flow for several hours at 700 °C until the excess oxygen was removed from the alloys and an equilibrium between the oxygen activities in the gas atmosphere and in the liquid alloys was achieved (measured oxygen partial pressure reached a constant value). Then, the temperature was decreased to the test temperature (450 °C for tests in $SbBi_9$, 420 °C for tests in Sb_2Bi_8, and 470 °C for tests in Sb_3Bi_7) and the test specimens were introduced. The test temperatures 470 °C and 420 °C were selected for the exposures to Sb_3Bi_7 and Sb_2Bi_8, respectively. These temperatures are 50 K above the respective melting temperatures of the alloys and, thus, represent reasonable working temperatures for an LMB. This reasoning results in a test temperature of 370 °C for $SbBi_9$. However, to explore the effect of alloy composition rather than the influence of temperature, an exposure temperature of 450 °C was chosen for $SbBi_9$.

For loading and unloading the specimens, a glovebox was pre-conditioned with Ar5%H_2 gas and connected to the quartz tube to maintain the atmosphere inside the tube. Each crucible was loaded with

Table 1
Composition of test materials as measured by SEM-EDS (in wt%).

Specimen	Co	Cr	Ni	Mn	Mo	Si	Fe
T91	-	8.8	0.04	0.4	2.5	0.4	Bal.
SS 316L-A	-	17.2	8.6	1.8	3.0	0.7	Bal.
SS 316L-B	-	15.1	14.8	1.6	3.1	1.2	Bal.
Kovar 4J29	17.6	-	28.1	0.1	-	0.4	Bal.

one test specimen. Each specimen was fixed to a sample holder by Mo wires to force the lower part of the specimen submerged in the liquid Sb-Bi alloy. The ratio of exposed specimen surface to liquid metal volume did not exceed 300 cm^2/L. After 740 h of exposure, the specimens were extracted from the crucibles and cooled down to room temperature in the controlled atmosphere of the glovebox. During the entire exposure test, the oxygen partial pressure remained below 10^{-34} bar at the test section.

2.3. Post-test analysis

The immersed part of all specimens was more or less covered by a layer of Sb-Bi alloy. Without further cleaning, all specimens were cut, embedded in resin, ground and polished to a diamond size of 1 µm. For cross-section examination, a scanning electron microscope (SEM, Zeiss LEO 1530 VP) equipped with an energy dispersive X-ray spectrometry (EDS) was used.

3. Results

3.1. Fe-Cr-Ni steel SS 316L

The surfaces of all SS 316L specimens are corroded after 740 h exposure to the different liquid Sb-Bi alloys, see Fig. 1 for an overview. Hereby, the position of the original sample surface was confirmed at the boundary between the part of the specimen exposed to the Sb-Bi alloy and the unexposed part, the latter not showing any corrosion. In case of $SbBi_9$/450 °C, some regions without corrosion attack are found. The corroded regions are composed of distinct layers (visible in the lower row of Fig. 1). The specific thicknesses and compositions of these layers depend on the exposure conditions, i.e., on the Sb-Bi alloy composition and exposure temperature, as discussed below. Sb-Bi alloy with corrosion products sticks to the sample surface (except at the uncorroded regions after exposure to $SbBi_9$). Hereby, depending on the exposure conditions, different corrosion products precipitated as solid phases on the sample surface.

Fig. 2 shows a closer look at the typical corrosion layers for all three exposure conditions, together with their compositions measured by EDS along the respective specified lines. The corrosion layers are characterized by large penetration of Sb and of the impurity As and by minor penetration of Bi into the steel in two or three distinct layers. A small signal from oxygen was also detected by EDS everywhere on the specimen, in particular in the bulk material. It is attributed to oxidation of the cross-section sample after its preparation. Therefore, the oxygen signal is omitted in the further analysis. This also applies to the other materials presented below.

Common to all exposures of SS 316L, an Sb- and Fe-rich layer forms at the corrosion front (denoted Cor1 in Fig. 2). In this layer, all steel alloying elements (Fe, Cr, Ni) are depleted compared with the bulk material. The Cr content shows a gradual decrease from ~12 at% at the corrosion front to ~5 at% at the end of this layer, Fe is either constant (~40 at%) or shows the opposite trend (increase from ~38–45 at%), and Sb has a roughly constant concentration of ~45 at%. Small amounts of Ni and Bi are found (~3 at%) in the entire layer, while As is detected only next to the adjacent corrosion layer and only in case of the exposure to $SbBi_9$/450 °C where the adjacent corrosion layer contains large amounts of As (see below). Additionally, Bi is found in some locations in high concentration, namely along cracks, at small spots within the Sb-Fe-rich layer Cor1, or along the corrosion front.

The atomic ratio of the elements Fe, Cr, and Sb in the first corrosion layer Cor1 suggests formation of the solid solution (Fe,Cr)Sb after all three exposure tests. At the given exposure temperatures, antimony is known to form the intermediate compounds FeSb (non-stoichiometric compound) and $FeSb_2$ (stoichiometric phase). Like the Fe-Sb system, also the binary system Cr-Sb forms the two stable phases CrSb (non-stoichiometric) and $CrSb_2$. Due to the similarity of Fe and Cr, the ternary system Fe-Cr-Sb exhibits solid solutions of the described binary compounds, i.e., (Fe,Cr)Sb and $(Fe,Cr)Sb_2$ [25].

In addition to the composition, also the thickness of the layer Cor1 at the corrosion front is very similar for the different exposure conditions, see Table 2. In case of Sb_3Bi_7/470 °C, the layer shows lateral cracks.

In contrast to the first corrosion layer Cor1, the different exposure conditions cause significant deviations in the composition and thickness of the second corrosion layer Cor2 that directly follows the (Fe,Cr)Sb layer (see Fig. 2). After exposure to $SbBi_9$/450 °C, an As-rich layer is observed. Its thickness is typically below 4 µm (Fig. 2(a)), but it can reach in some areas up to 20 µm, see Fig. 3(a). This layer mainly consists of As (~35 at%), Fe (~40 at%), and Cr (~25 at%), with the latter even

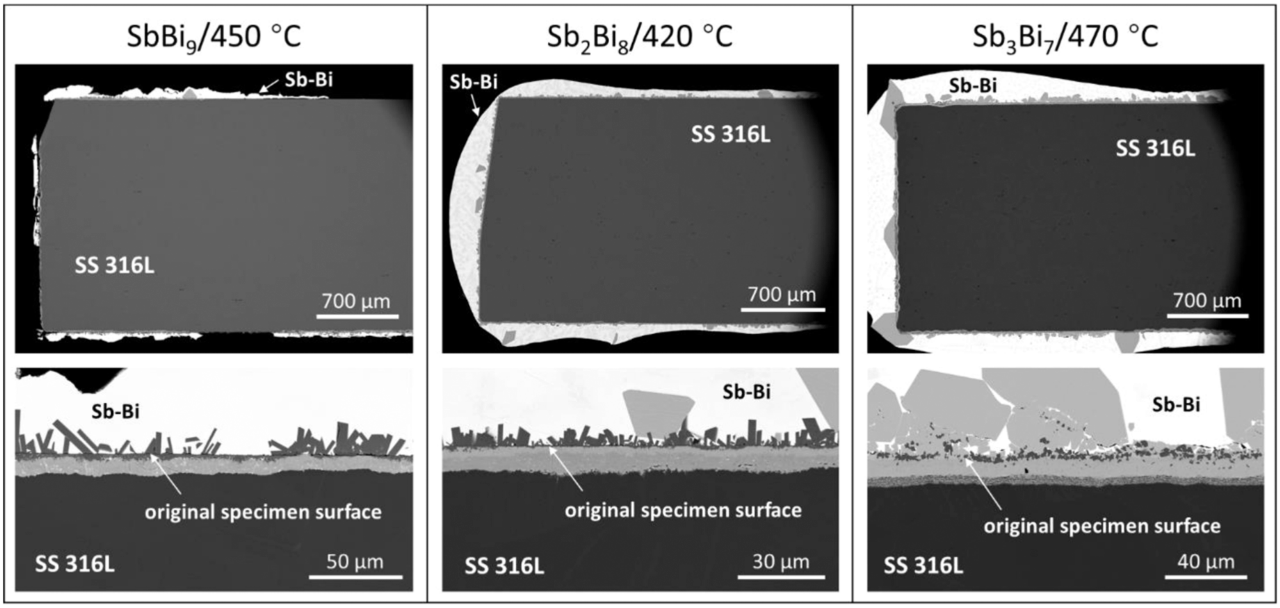

Fig. 1. SEM/BSE images of SS 316L after 740 h exposure to liquid Sb-Bi alloys with three different compositions as indicated. The upper row shows the entire bottom part of the sample that was submerged in the liquid Sb-Bi alloy, the lower row shows a typical section of the corroded sample surface together with adherent Sb-Bi alloy.

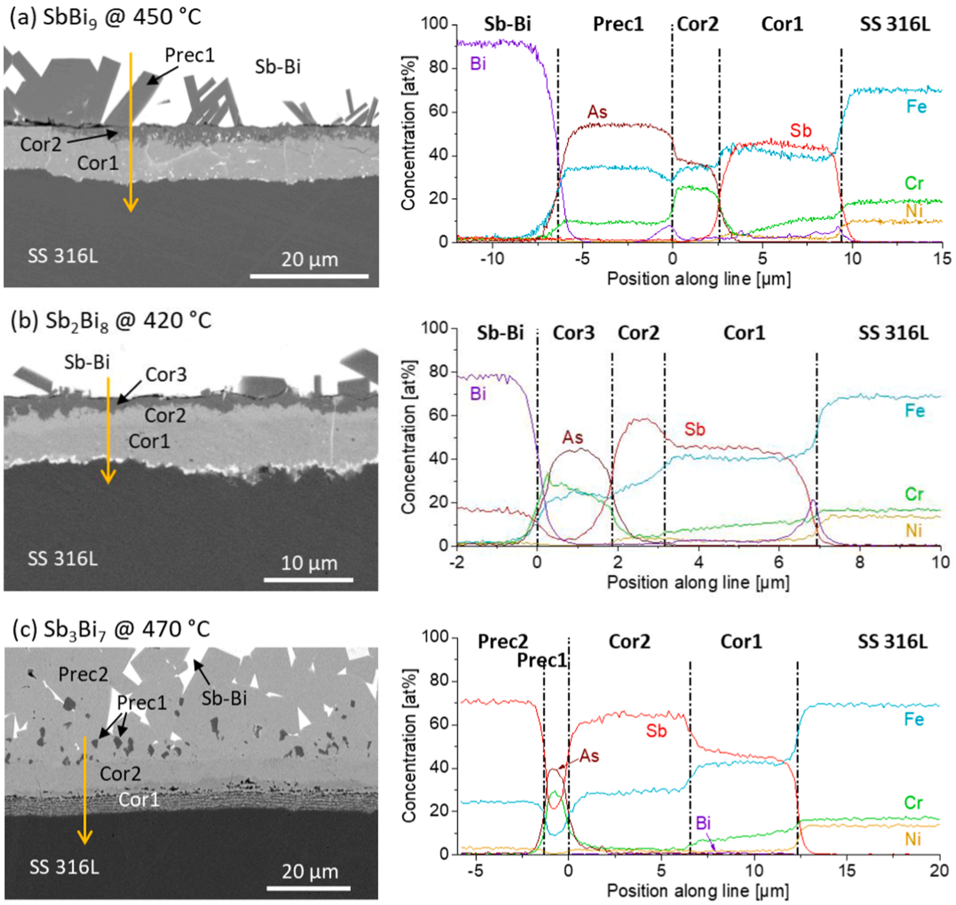

Fig. 2. Typical corrosion behavior of SS 316L after exposure to (a) $SbBi_9$/450 °C, (b) Sb_2Bi_8/420 °C, and (c) Sb_3Bi_7/470 °C. For each exposure condition, an SEM/BSE image is shown on the left and the EDS elemental composition along the specified line is displayed on the right. The position 0 on the x-axes corresponds to the original sample surface. The different corrosion layers are denoted Cor1 etc., while precipitates are named Prec1 etc.

Table 2
Proposed main compound and thickness (in µm) of distinct corrosion layers of SS 316L after 740 h exposure to Sb-Bi alloys. Values of local behavior in brackets.

layer	$SbBi_9$/450 °C		Sb_2Bi_8/420 °C		Sb_3Bi_7/470 °C	
	compound	thickness	compound	thickness	compound	thickness
Cor1	(Fe,Cr)Sb	6.5–9	(Fe,Cr)Sb	4.5–7	(Fe,Cr)Sb	4–7.5
Cor2	$(Fe,Cr)_2As$	0–4 (up to 20)	$FeSb_2$	1–2 (0)	$FeSb_2$	5–11
Cor3	-	-	(Fe,Cr)As	1–3 (up to 25)	-	-

exceeding the bulk value of the steel. The As-Fe binary system shows three stable intermediate compounds at the exposure temperature, namely Fe_2As, FeAs, and $FeAs_2$ [26]. Similarly, the As-Cr system forms stable intermediate compounds, including Cr_3As, Cr_2As, CrAs, and $CrAs_2$, where the latter requires high pressure for formation [27]. The measured atomic ratio of the elements suggests formation of $(Fe,Cr)_2As$, i.e., a solid solution of the intermetallic compounds Fe_2As and Cr_2As.

In case of exposure to Sb_2Bi_8 at 420 °C, the layer Cor2 shows even higher Sb content than Cor1 and is followed by an As-rich third corrosion layer Cor3 located at the sample surface, see Fig. 2(b). Although these two layers are typically rather thin (1–2 µm each), probably due to the lower exposure temperature, the elemental compositions indicate formation of $FeSb_2$ and of the solid solution (Fe,Cr)As, respectively, in the intermediate layer Cor2 and in the top-most layer Cor3. In some locations, the (Fe,Cr)As layer Cor3 can reach up to 25 µm thickness, see Fig. 3(b). In such places, the intermediate $FeSb_2$ layer Cor2 is not observed.

Exposure to Sb_3Bi_7 at 470 °C leads to formation of a well-developed Sb-rich layer Cor2 that follows the (Fe,Cr)Sb layer Cor1 at the corrosion front (Fig. 2(c)). The layer Cor2 contains neither high As concentrations nor high amounts of Cr. Instead, a 5–11 µm thick layer with ~64 at% Sb and ~28 at% Fe is formed. The composition suggests formation of $FeSb_2$. Although small As-rich precipitates are found along the sample surface (Prec1), the As-rich phase does not penetrate the steel as in case of $SbBi_9$ and Sb_2Bi_8. Furthermore, no local deviations from the described behavior are observed, neither in composition of the distinct corrosion layers nor in thickness.

As already mentioned, corrosion products are precipitated in the Sb-Bi alloy that sticks to the sample surface. After exposure to $SbBi_9$/450 °C, many As-rich elongated “dendrites” with a composition of ~53 at% As, ~35 at% Fe, and ~10 at% Cr are found (Prec1 in Fig. 2(a)). After exposure to Sb_3Bi_7/470 °C, on the other hand, large regions (tens of µm) of an Fe-rich Sb phase with ~70 at% Sb, ~25 at% Fe, and ~3 at% Ni are observed almost everywhere along the sample surface (Prec2 in Fig. 2(c)). Exposure to Sb_2Bi_8, i.e., the composition between the other two Sb-Bi alloys, results in some As-rich elongated “dendrites” and some large regions with the Fe-rich Sb phase, see Fig. 1.

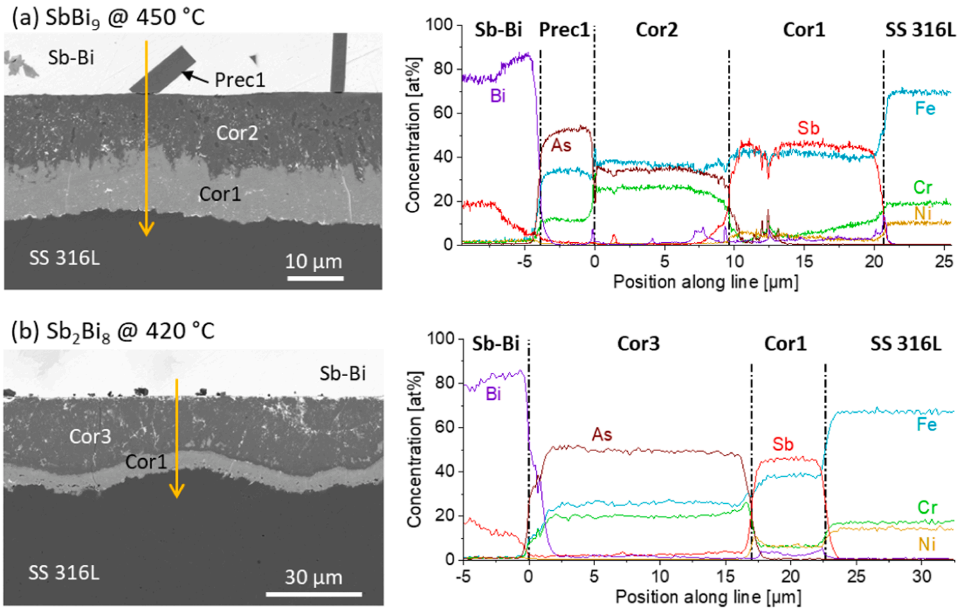

Fig. 3. Deviating corrosion behavior of SS 316L after exposure to Sb-Bi alloys, together with composition along specified lines. Further details as given in Fig. 2.

3.2. Fe-Cr steel T91

Similar to the Fe-Cr-Ni austenitic steel SS 316L, also the Fe-Cr ferritic steel T91 shows a generally homogeneous corrosion attack after 740 h exposure to Sb-Bi alloys with different compositions, see Fig. 4. Although there are some local deviations, the thickness of the corrosion layer remains below a corrosion depth of 40 µm. The corrosion attack is composed of distinct layers. The homogeneity, thickness, and composition of the corrosion layers depends on the exact exposure conditions as described in the following.

A more detailed SEM/EDS analysis of the corrosion attack of T91 after the different exposure tests is shown in Fig. 5. It reveals for all exposure conditions a diffusion zone (Diff) of antimony along preferred paths into the pristine steel at the corrosion front, followed by the already familiar Sb-Fe-rich layer Cor1. The thickness of the Sb diffusion zone depends on the exposure conditions and reaches a depth of 3 µm (see Table 3); it was not observed for SS 316L. The Sb-Fe-rich layer Cor1 exhibits a rather homogeneous thickness and is mainly composed of Sb and Fe (each around 40–45 at%) and some Cr (<5 at%). As for SS 316L, this suggests formation of the solid solution (Fe,Cr)Sb of the two non-stoichiometric intermediate phases FeSb and CrSb, although the Cr content is lower (and the Fe content correspondingly higher) than in case of SS 316L. In contrast to SS 316L, the (Fe,Cr)Sb layer at the corrosion front of T91 is not cracked laterally after exposure to Sb_3Bi_7/470 °C.

The properties of the second corrosion layer Cor2 of T91 succeeding the (Fe,Cr)Sb layer Cor1 depend on the exposure conditions in a way similar to SS 316L. After exposure to $SbBi_9$/450 °C, the second corrosion layer of T91 is generally rather thin and shows patches of different compositions, see Cor2 and Cor3 in Fig. 5(a). In some locations, an

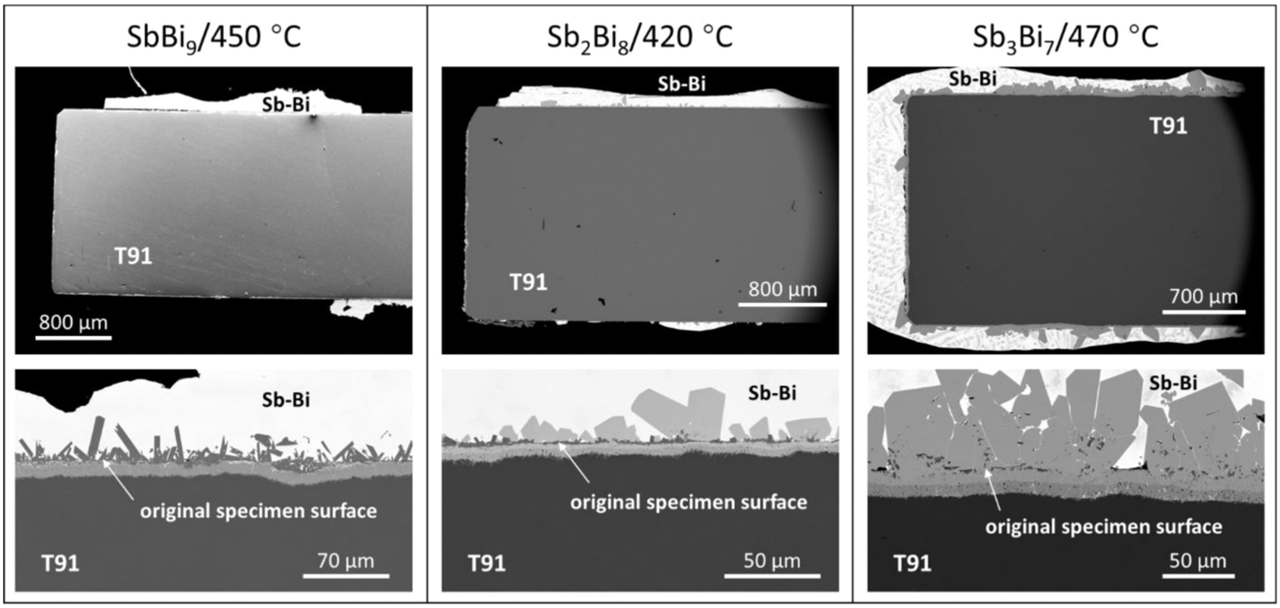

Fig. 4. SEM images (first: SE, all others: BSE) of T91 ferritic steel after 740 h exposure to liquid Sb-Bi alloys with three different compositions. Further details as given in Fig. 1.

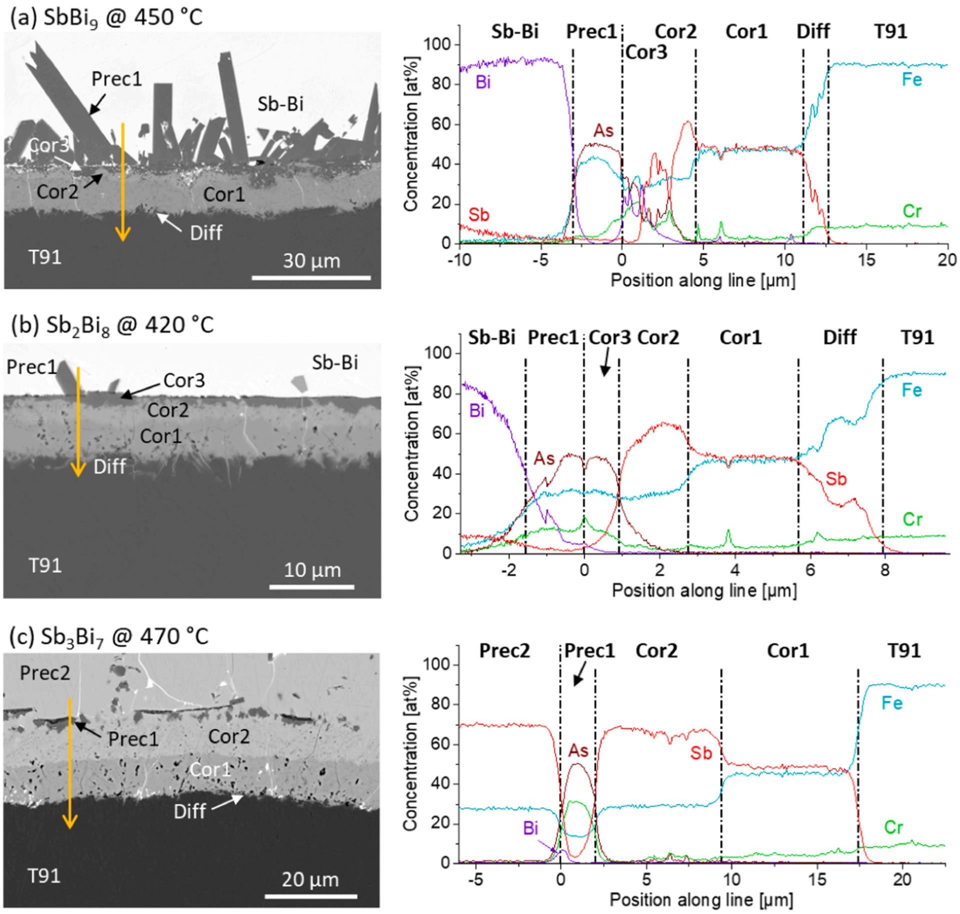

Fig. 5. Typical corrosion behavior of T91 after different exposure tests, together with elemental composition along specified lines. Diff denotes Sb diffusion into the steel. Further details as given in Fig. 2.

Table 3
Proposed main compound and thickness (in µm) of distinct corrosion layers of T91 after 740 h exposure to Sb-Bi alloys. Values of local behavior in brackets.

layer	$SbBi_9$/450 °C		Sb_2Bi_8/420 °C		Sb_3Bi_7/470 °C	
	compound	thickness	compound	thickness	compound	thickness
Diff		up to 2.5		up to 3		up to 1.5
Cor1	(Fe,Cr)Sb	7–9	(Fe,Cr)Sb	3–4.5	(Fe,Cr)Sb	6.5–9.5
Cor2	$FeSb_2$	0–2 (0)	$FeSb_2$	0.5–3.5	$FeSb_2$	6.5–10
Cor3	$(Fe,Cr)_2As$	0–4 (up to 18)	(Fe,Cr)As	0–2	-	-
	Bi-rich	- (up to 30)				

extended $(Fe,Cr)_2As$ layer Cor3 is obtained (as for SS 316L) with strong variations in thickness up to 18 µm (Fig. 6(a)). In these locations, the layer Cor2 is entirely missing. Compared with SS 316L, the ratio of Fe to Cr is shifted in case of T91 towards Fe. In addition, the $(Fe,Cr)_2As$ layer Cor3 of T91 is penetrated to a higher extent by Bi. In some locations, this even results in large corrosion regions with depths up to 30 µm (Fig. 6 (b)).

Exposure of T91 to Sb_2Bi_8 at 420 °C (Fig. 5(b)) leads to an intermediate $FeSb_2$ layer (Cor2) and an (Fe,Cr)As layer at the sample surface (Cor3) as was observed for SS 316L. Again, the Fe content is higher at the expense of a lower Cr content compared with SS 316L. In contrast to SS 316L, the (Fe,Cr)As layer remains below a thickness of 2 µm throughout the entire surface of T91.

As for SS 316L, exposure of T91 to Sb_3Bi_7 at 470 °C leads to a second corrosion layer that consists of $FeSb_2$, and small As-rich precipitates are found along the initial sample surface, see Fig. 5(c).

On the sample surface, As-rich precipitates (Prec1) with ~50–55 at% As and ~40–45 at% Fe have grown after exposure to $SbBi_9$ at 450 °C. As already observed for the (Fe,Cr)Sb layer at the corrosion front and the As-rich layers, also the As-rich precipitates Prec1 of T91 have a lower Cr content and a higher Fe content compared with SS 316L. After exposure to Sb_3Bi_7 at 470 °C, solid regions (Prec2) with ~70 at% Sb and ~30 at% Fe are attached to the sample surface. After exposure of T91 to Sb_2Bi_8, both features, i.e., As-rich precipitates Prec1 and the precipitated Fe-rich Sb phase Prec2, are found embedded in Sb-Bi alloy along the sample surface, although in lower amounts.

3.3. Fe-Co-Ni alloy Kovar 4J29

In contrast to the rather thin and compact corrosion layers observed for the steels, Kovar 4J29 exhibits a deep corrosion attack with a porous structure after 740 h exposure to liquid Sb-Bi alloys. As illustrated in Fig. 7, the depth of the corrosion attack and the size of the pores strongly depend on the exposure conditions, in particular on the Bi content of the Sb-Bi alloy. A corrosion depth of about 800 µm is observed after exposure to $SbBi_9$/450 °C (only the region in the center of the specimen

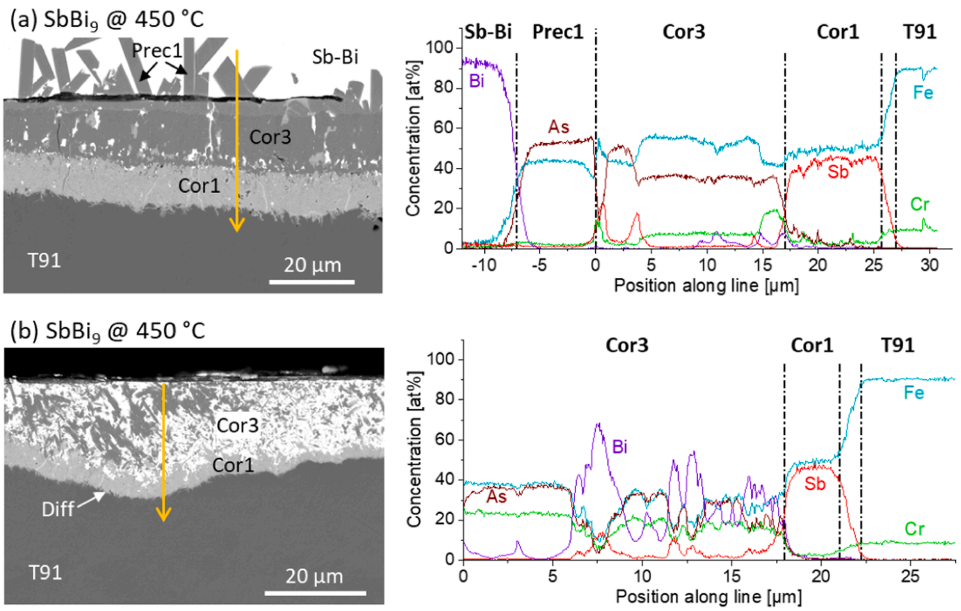

Fig. 6. Deviating corrosion behavior of T91 after exposure to SbBi$_9$ at 450 °C, together with composition along specified lines. Further details as given in Fig. 2.

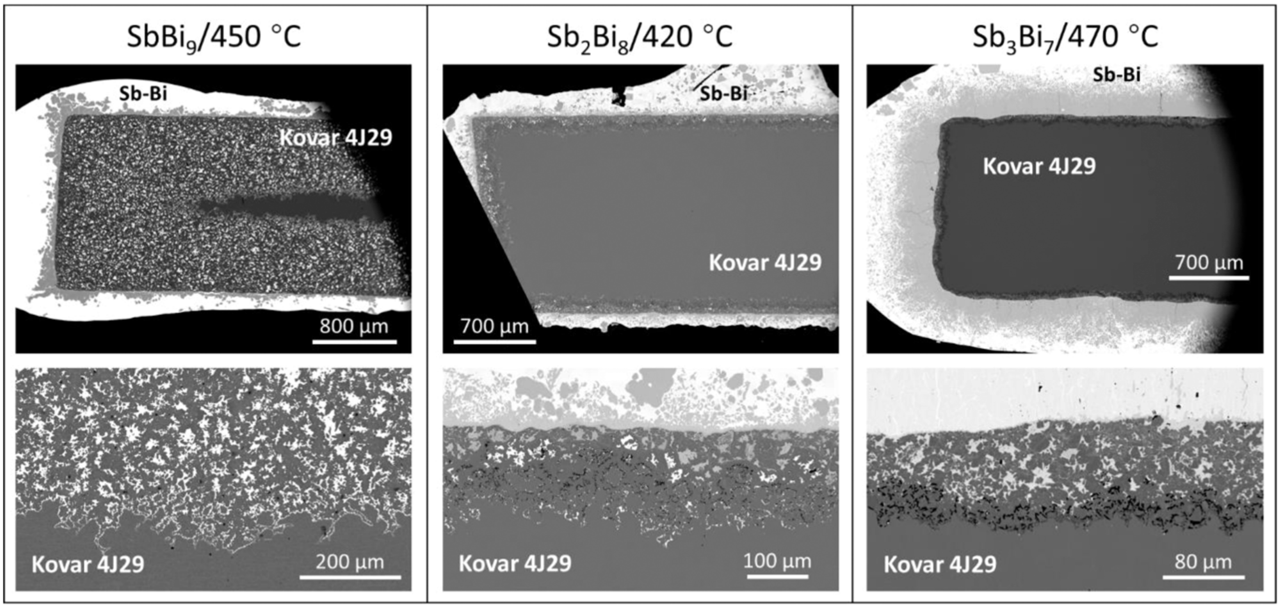

Fig. 7. SEM/BSE images of Kovar 4J29 after 740 h exposure to different liquid Sb-Bi alloys. Further details as given in Fig. 1. The lower left picture shows the corrosion front.

remains uncorroded), while the corrosion layer reaches only ~100 µm for exposure to Sb$_3$Bi$_7$/470 °C. However, in the latter case the sample surface shows a recession of ~50 µm (determined from the comparison with the unexposed part of the sample) in addition to the ~100 µm corrosion layer, while no recession is observed after exposure to SbBi$_9$/450 °C. For all exposures, the pores are smallest at the corrosion front and increase in size with increasing distance from the corrosion front. The largest pores are observed close to the sample surface after exposure to SbBi$_9$/450 °C. In all three cases, Sb-Bi alloy with corrosion products sticks on the sample surface.

A closer look by SEM at the corrosion attack of Kovar 4J29 by the different Sb-Bi alloys is presented in Fig. 8, including information about the composition of the different regions as determined by EDS.

For SbBi$_9$/450 °C exposure, the darkest regions in Fig. 8(a), denoted as Cor, show the remains of Kovar with a strong reduction of the Ni contents compared with the original material (28 at% Ni). Sb and Bi are hardly detected here. The bright regions in the corrosion attack are pores filled with Bi (Pore). Bi-filled pores are found throughout the entire corrosion attack. The medium-dark regions (Prec1), which appear only along the specimen surface both inside the pores and as precipitates on the sample surface, show high Sb (~55 at%) and Ni (~40 at%) content as well as some Fe (<5 at%). The binary system Ni-Sb is known to form the stable intermetallic compounds Ni$_3$Sb, Ni$_7$Sb$_3$, NiSb (non-stoichiometric), and NiSb$_2$ at the given temperature of 450 °C. Thus, the measured composition of the Sb-Ni-rich phase Prec1 suggests presence of NiSb$_2$ and NiSb. Arsenic is not found anywhere in the corrosion attack.

After exposure to Sb$_2$Bi$_8$ at 420 °C, the corroded porous structure of Kovar 4J29 is 120–180 µm thick. The remaining Kovar material (Cor in Fig. 8(b)) shows a strong depletion in Ni in the entire corrosion layer

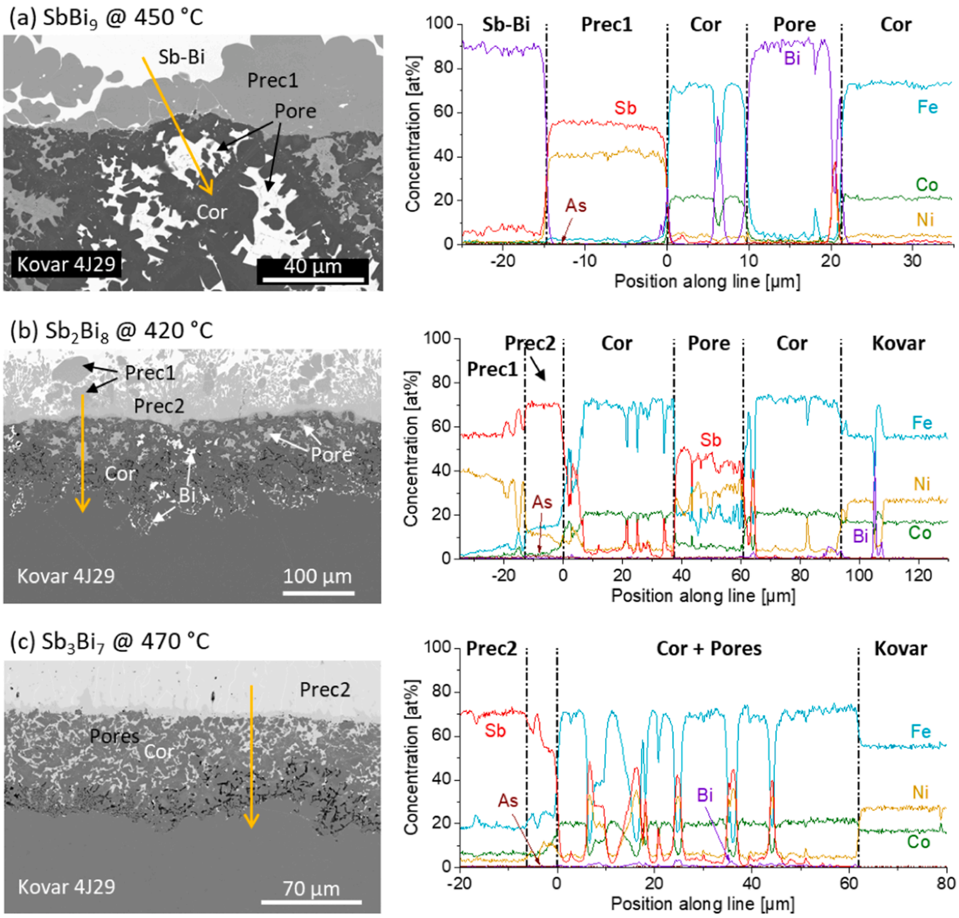

Fig. 8. Corroded regions of Kovar 4J29 after exposure to different Sb-Bi alloys, together with composition along specified lines. Further details as given in Fig. 2.

(~5 at% Ni) as was observed after exposure to $SbBi_9$. In contrast to $SbBi_9$-exposure, however, significant amounts of Sb (~5 at%, locally up to 20 at%) penetrated the Ni-depleted Kovar material Cor close to the surface. The pores show different characteristics in different depths: at the corrosion front, they are small and filled with Bi; at intermediate depths, in a band from ~60 to ~100 µm, the pores are still small but mainly empty; in the outer-most regions, larger pores are obtained, which are filled either with Bi or an Sb-Ni-rich phase (~45 at% Sb, ~30 at% Ni, ~20 at% Fe, ~6 at% Co), see Pore in Fig. 8(b). The precipitated material that sticks on the sample surface comprises some darker patches (Prec1) embedded in a slightly brighter matrix (Prec2). The composition of the darker Prec1 patches (~55 at% Sb, ~40 at% Ni) resembles the medium-dark regions found along the sample surface after exposure to $SbBi_9$/450 °C (Prec1 in Fig. 8(a)). The majority of the precipitated/solid material Prec2 that directly sticks on the sample surface after exposure to Sb_2Bi_8, however, shows a slightly different composition with even higher Sb content but less Ni (~70 at% Sb, ~15 at% Fe, ~11 at% Ni). Regions with this composition were not observed after exposure to $SbBi_9$.

The corrosion layer of Kovar 4J29 after exposure to Sb_3Bi_7/470 °C is also composed of pores and remains of the original materials and reaches a depth of 80–120 µm, see Fig. 8(c). The remaining Kovar alloy is strongly depleted in Ni (~5–6 at%) compared with the uncorroded material as was observed for the other two exposures. Similar to the exposure to Sb_2Bi_8, Sb penetrates the Ni-depleted remains of Kovar; its content increases from 0 at the corrosion front to ~5 at% close to the sample surface. As for exposure to Sb_2Bi_8, not all pores are filled after exposure to Sb_3Bi_7. In the first ~20–40 µm along the corrosion front, mainly empty pores are obtained (except for one location where Bi penetrates the pores and accumulates at the corrosion front, most probably due to a crack in the material that sticks on the sample surface). In the remaining corrosion layer, the pores are filled with an Sb-rich phase with ~45 at% Sb, ~35 at% Ni, and ~10 at% Fe. The large continuous region attached to the sample surface (Prec2) shows ~70 at% Sb, ~18 at% Fe, ~6 at% Co, and ~3 at% Ni. This composition resembles, regarding the high Sb content, the patches Prec2 attached on the sample exposed to Sb_2Bi_8 (Fig. 8(b)). As for the samples exposed to $SbBi_9$ and Sb_2Bi_8, no arsenic is found in/on the Kovar specimen after exposure to Sb_3Bi_7.

3.4. Mo metal

As shown in Fig. 9, Mo metal retains its original shape after exposure to liquid Sb-Bi alloys. However, Sb-Bi alloy sticks to its surface in most areas, which indicates some reaction between the liquid metal and Mo.

Fig. 10 shows the interface between Mo and the Sb-Bi alloy at higher magnification, together with EDS elemental line scans across this interface. After all three exposures, an enrichment of As is found at the surface of Mo. For exposure to both $SbBi_9$ and Sb_2Bi_8, the As content slowly increases from the Sb-Bi alloy side, has its maximum on the Mo side of the original interface (at about 0.3 µm depth), and then quickly decreases to zero. For Sb_3Bi_7 exposure, a clearly pronounced distinct Mo-As layer, about 1 µm thick, has developed along the entire sample surface. The asymmetry of the As profile and the broadened profiles of Bi and Mo at the Mo-alloy interface indicate interdiffusion of Bi and Mo. The As- and Mo-profiles at the penetration front of As into the Mo material are much steeper, possibly limited in steepness only by the limited spatial resolution due to the finite interaction volume of the penetrating 20 keV beam electrons into the material. The non-zero Bi signal inside the bulk of Mo stems from the close proximity of the BiM (2.419 keV)

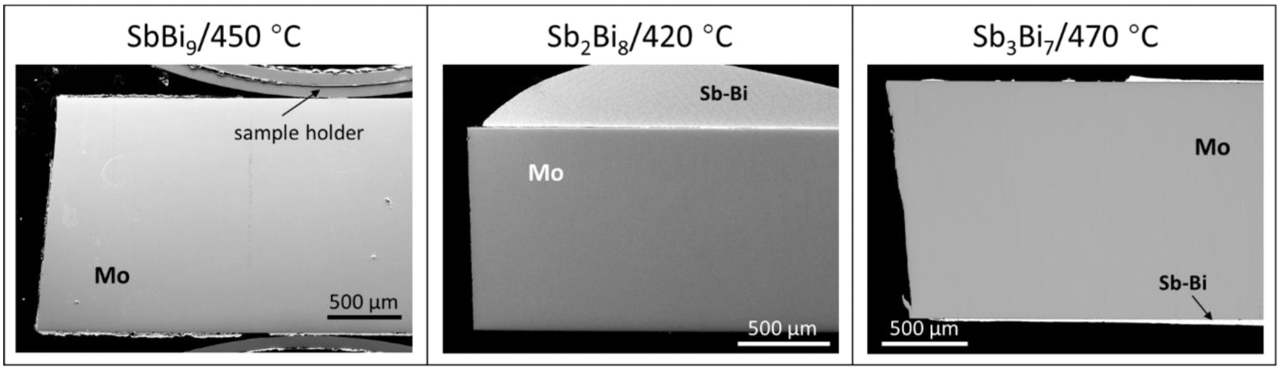

Fig. 9. SEM images (first and second: SE, third: BSE) of Mo metal after 740 h exposure to different liquid Sb-Bi alloys as indicated. The pictures show the entire bottom part of the sample that was submerged in the liquid Sb-Bi alloy.

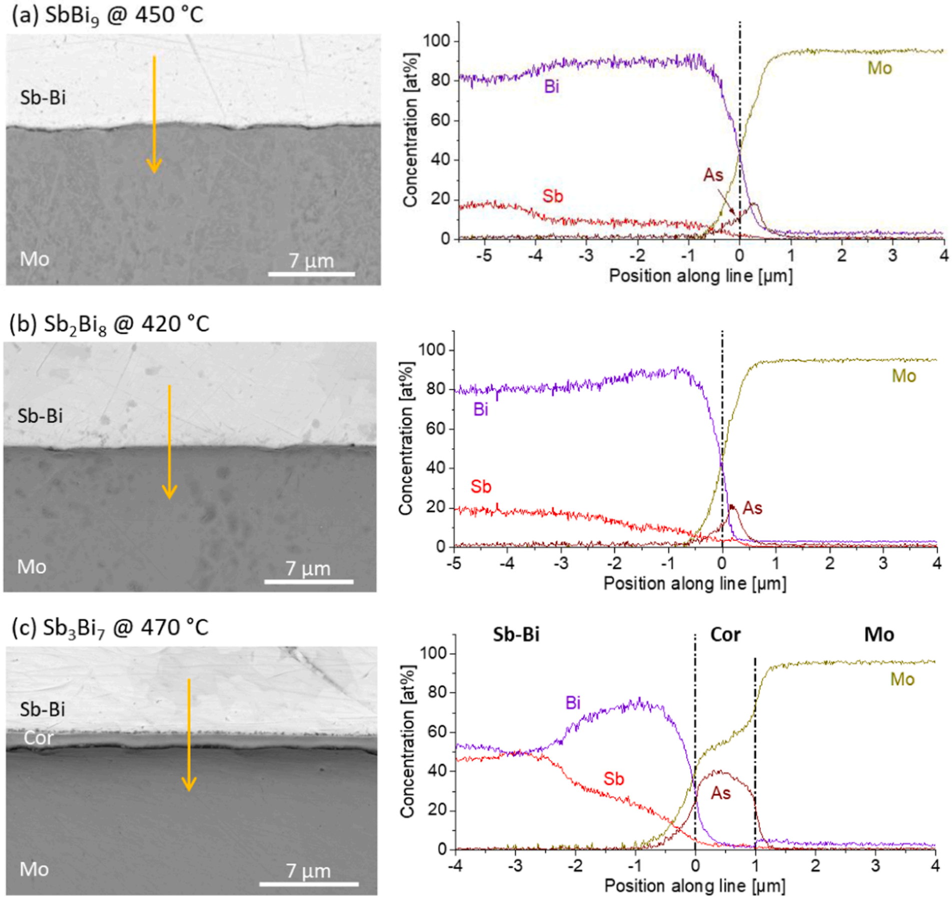

Fig. 10. Mo/Sb-Bi interface after exposure to different Sb-Bi alloys, together with composition along specified lines. Further details as given in Fig. 2.

and MoLa (2.293 keV) characteristic peaks in the X-ray spectrum.

4. Discussion

For all Sb-Bi alloys tested, Mo exhibits the best corrosion resistance, the steels SS 316L and T91 show moderate corrosion depths (in the range 10–20 µm after 740 h at ~450 °C), and the most severe corrosion attack with several 100 µm depth is found for Kovar. None of the materials shows formation of an oxide on its surface. This confirms that, as intended, the oxygen content of the liquid Sb-Bi alloys was sufficiently low to have no influence on the corrosion process. This mimics the situation in a hermetically closed liquid metal battery, where any oxygen impurity present during cell assembly, either in the gas atmosphere or as natural oxide layer on the materials' surfaces, is consumed by the strongest oxide formers (typically Li) until an equilibrium of the oxygen potentials is achieved. After some potential influence of oxygen on a short timescale, oxygen does not participate in the corrosion process of PCC materials in an LMB cell.

4.1. Kovar

Kovar 4J29 is the only material that shows regions with total dissolution (Figs. 7 and 8). Responsible is the high solubility of both Ni and Co in Bi, two alloying elements with high concentration in Kovar

(Table 1). Calculations based on the solubility in Bi show that dissolution depths of around 2 mm and 6 mm, respectively, are required to reach the solubility limits of Ni and Co in the Sb-Bi alloys at the given ratio of exposed specimen surface to Sb-Bi alloy volume. Thus, neither Ni nor Co reach saturation during the course of the experiment. For Fe, which has only moderate solubility in Bi, the situation is different and the solubility limit is reached after a rather short time. It is estimated that the Sb-Bi alloys are saturated in Fe for a dissolution depth of only around 0.1 μm. Nevertheless, dissolution of Fe proceeds beyond the solubility limit due to formation of solid Fe-Sb compounds (potentially far away from the sample surface). The observed porous structure of the corroded Kovar material (Fig. 8) suggests that the corrosion process starts with selective dissolution of Ni in the entire corrosion attack, followed by total dissolution of the remaining Ni-depleted Kovar material. The total dissolution begins at the corrosion front with a branched, dendritic-type growth of pores, which then increase in size as the exposure to the liquid Sb-Bi alloy proceeds. Depending on the Sb-Bi alloy composition, different scenarios occur in the pores and on the sample surface.

In case of $SbBi_9$, all pores are filled with Bi, which results in proceeding pore formation at the corrosion front and pore growth in the entire corroded region. As a consequence, a corrosion depth of ~800 μm depth is obtained after 740 h at 450 °C. In some but not all regions along the specimen surface, a Sb-Ni-rich compound precipitates on the sample surface and in the pores. This compound forms individual patches that cannot prevent the transport of Bi into the sample and of dissolved Ni, Co, and Fe out of the sample.

When Kovar is exposed to Sb_2Bi_8, an Sb-rich phase (Sb-Fe-Ni-Co compound, ~70 at% Sb) precipitates around the Kovar specimen in addition to some patches of the Sb-Ni-rich compound. The Sb-rich phase forms many small patches detached from the sample surface, but also a thin (~10 μm) continuous layer along the sample surface. This compact layer seems to act as barrier that mitigates the exchange of material. As a consequence, only few pores are filled with Bi and the corrosion attack is less deep (about 150 μm after 740 h at 420 °C). Note that the corrosion depth is additionally reduced by the slightly lower test temperature. An Sb-Ni-rich phase is found in the pores close to the sample surface.

After exposure to Sb_3Bi_7, the Kovar specimen is surrounded by a 400 μm thick layer of an Sb-rich phase (Sb-Fe-Ni-Co compound, ~70 at % Sb). This layer is compact in the first ~200 μm and becomes fragmented further away from the specimen surface. The compact part is even more effective in mitigating material transport than the corresponding thin layer after exposure to Sb_2Bi_8. In case of Sb_3Bi_7, no Bi penetrates the pores and the depth of the corroded layer is with ~100 μm (plus ~50 μm material recession) not larger than in case of Sb_2Bi_8, despite the higher exposure temperature of 470 °C.

At higher temperature, the rate of both dissolution and compound formation is increased due to a higher solubility and accelerated kinetics. Although the higher temperature of the Sb_3Bi_7/470 °C test could be, in principle, solely responsible for the thicker layer of the Sb-rich phase and, thus, better dissolution mitigation, the temperature effect cannot explain the significantly better corrosion resistance of Kovar 4J29 in Sb_2Bi_8/420 °C compared with $SbBi_9$/450 °C.

To summarize, at temperatures around 450 °C, the content of Sb in the Sb-Bi alloy determines whether and to which extent a compact Sb-rich layer forms on the sample surface and mitigates the severe dissolution attack of Kovar 4J29. The corrosion-mitigating Sb-rich layer contains some Fe, Ni, and Co, and ~70 at% Sb and is thicker and, thus, more effective for higher Sb content in the Sb-Bi alloy. The influence of the temperature variations in the range 420–470 °C is outbalanced by the described impact of the Sb content.

The observed corrosion behavior of Kovar might well be influenced by the limited amount of Sb-Bi alloy used in the experiments, which results in Fe saturation as discussed above and facilitates the formation of solid Sb-compounds. An orders-of-magnitude lower ratio of exposed surface to Sb-Bi alloy volume could retard the formation of corrosion-mitigating Sb-compounds, thus leading to a more severe dissolution corrosion also in case of Sb_2Bi_8 and Sb_3Bi_7. Precondition for such an influence of the alloy volume, however, is a fast enough transport (diffusive or convective) of dissolved Fe in the Sb-Bi alloy to avoid local oversaturation. Note that the surface to volume ratio used in the current study roughly corresponds to the situation in a typical liquid metal battery.

4.2. Steels

Regarding the investigated steels, the corrosion attack by Sb-Bi alloys consists of two or three distinct layers with different compositions. Hereby, great similarities are found between SS 316L and T91 regarding the type and composition of these layers. For both steels and all three exposure tests, the Fe content of the distinct corrosion layers decreases stepwise from the bulk towards the Sb-Bi alloy. The Fe-Cr-Ni steel 316L is strongly depleted in Ni in the entire corroded layer. This suggests that the corrosion process of SS 316L involves strong selective dissolution of Ni into the Sb-Bi alloy, caused by the high solubility of Ni in Bi. As for Kovar, the solubility limit of Ni in the Sb-Bi alloy is not reached in the course of the exposure test. For SS 316L, dissolution to a depth of around 5–7 mm would be required to reach this limit at the given surface to volume ratio. Despite the very dissimilar Ni contents of stainless steel 316L and the Fe-Cr ferritic steel T91, similar corrosion depths are obtained for these two classes of steel (Tables 2 and 3). Likewise, no differences in the corrosion behavior of SS 316L could be identified that is attributable to the differences in Ni content between SS 316L-A and SS 316L-B (Table 1). This indicates that Ni dissolution is not the rate-determining step of the underlying corrosion mechanism. Once SS 316L is depleted in Ni due to selective dissolution into the Sb-Bi alloy, the main difference in composition between both SS 316L materials and T91 is the higher Cr content of SS 316L. Therefore, it does not surprise that the distinct corrosions layers of SS 316L (Fig. 2) contain a higher amount of Cr at the cost of a lower Fe content compared with the corresponding corrosion layers of T91 (Fig. 5). Apart from the composition, austenitic SS 316L and ferritic T91 deviate in their microstructure. This explains the observed diffusion of Sb along preferred paths into the pristine material at the corrosion front of T91 and its absence in case of SS 316L.

For all exposure conditions, the solid solution (Fe,Cr)Sb, i.e., an Fe-Cr-Sb compound, is found in a first layer at the corrosion front. This layer has a thickness in the range 3–9 μm, with the smallest values found for the exposure to Sb_2Bi_8/420 °C, most probably due to the slightly lower exposure temperature. Generally, this first layer is followed by a second corrosion layer composed of the intermetallic compound $FeSb_2$. Its thickness and stability depend strongly on the exposure conditions, in particular on the composition of the Sb-Bi alloy. After exposure to Sb_3Bi_7, the second layer shows with 8±3 μm for both steels the highest thickness of all exposures. The thickness of the $FeSb_2$ layer is strongly reduced to 2±1.5 μm after exposure to Sb_2Bi_8. Additionally, it becomes less stable, i.e., arsenic penetrates the steel (in case of SS 316L few local deeper attacks are observed, see Fig. 3(b)) and the solid solution (Fe,Cr) As replaces the $FeSb_2$ layer. Taking into account the replacement by (Fe, Cr)As, the hypothesized thickness of the $FeSb_2$ layer after exposure to Sb_2Bi_8 in the absence of As can be estimated as 3–4 μm for both steels. Finally, in the case of $SbBi_9$, no (SS 316L) or weak (T91) remnants of $FeSb_2$ are found. Both steels show several local deeper corrosion attacks (up to 30 μm) with strong penetration of As and/or Bi, see Fig. 3(a) and Fig. 6. The correlation between the existence and thickness of the $FeSb_2$ layer on the one hand and the occurrence of As and/or Bi penetration with deeper attack on the other hand suggests that the $FeSb_2$ layer has a mitigating effect on the penetration of As and/or Bi. Its formation is promoted by a higher activity/concentration of Sb in the Sb-Bi alloy as discussed below. However, the comparison with Kovar leads to the conclusion that the most effective layer in mitigating dissolution corrosion is the Fe-Cr-Sb compound at the corrosion front. Even in locations where the $FeSb_2$ layer fails, the corrosion depth does not exceed 30 μm thanks to a still intact Fe-Cr-Sb layer. Kovar, not containing any Cr, shows an 800 μm deep attack under the same conditions.

Regarding the underlying corrosion mechanism of steels in Sb-Bi alloys leading to the described distinct corrosion layers (Fe-Cr-Sb compound at the corrosion front, $FeSb_2$ intermetallic layer at the sample surface), one may think of several scenarios. One scenario is that the Fe-Cr-Sb layer grows inwards while the $FeSb_2$ layer grows outwards, similar to a bilayer oxide scale consisting of an inward-growing spinel and an outward-growing magnetite scale. Precondition for such a scenario is that both layers are permeable for Sb, Fe, and Ni, but not for Cr. However, the present experiments show high Cr content outside both corrosion layers (see As-rich compounds), clearly demonstrating permeability of the corrosion layers also for Cr. In addition, the interface between the two layers does not correspond to the original sample surface: firstly, it is not straight and precise but irregular and corrugated and secondly, it is not in line with the original sample surface still present at the part of the sample that was not exposed to the Sb-Bi alloy during the corrosion test. Instead, the surface of the $FeSb_2$ intermetallic layer shows all mentioned characteristics of an original sample surface. Both observations, the position of the original sample surface and the presence of substantial amounts of Cr beyond the corrosion layers, agree with the following proposed scenario of inward-growing layers as schematically drawn in Fig. 11. The corrosion layers are permeable for Sb, Fe, Ni, and Cr. The steel constituents diffuse outwards and dissolve in the Sb-Bi alloy, while Sb penetrates and forms (Fe,Cr)Sb at the corrosion front where the Sb activity is low. Because the Sb activity increases towards the sample surface, the Sb activity is somewhere inside the corrosion layer high enough to form $FeSb_2$ from the (Fe,Cr)Sb compound. The higher the Sb activity in the Sb-Bi alloy is, the further away from the sample surface this transition occurs, i.e., the thicker is the formed $FeSb_2$ layer. Fe and Cr liberated by the transition from (Fe,Cr)Sb to $FeSb_2$ also diffuse outwards and are dissolved in the liquid Sb-Bi alloy, where they form precipitates once the solubility limit is reached. As for Kovar, also for the steels the Sb-Bi alloy is saturated in Fe after total dissolution to a depth of around 0.1 μm. With partial dissolution, the required dissolution depths are accordingly larger. Nevertheless, the solubility limit is reached in the course of the exposure tests and formation of precipitates in the vicinity of the sample surface is promoted. In contrast to Kovar, however, these precipitates do not form a dense layer and are therefore not expected to have a strong influence on the proceeding corrosion process.

The corrosion thickness of 10–20 μm of both SS 316L and T91 after 740 h exposure to Sb-Bi alloys at temperatures in the range 420–470 °C compares well with the corrosion thickness of SS 301 and SS 430 in Sb_3Pb_7 at 450 °C (both ~10 μm after 500 h) reported in literature [21]. This further confirms that, although the solubilities of Fe, Cr, and Ni are much higher in Bi than in Pb, dissolution plays an inferior role even when exposed to Sb-Bi alloys with high Bi content because of the formation of a corrosion-mitigating layer composed of Fe-Sb and Fe-Cr-Sb compounds. The corrosion thickness in Sb-Bi alloys is also similar to results reported for ternary Sb-Bi-Sn alloys (16–32 μm after 500 h at 500 °C) [22]. In Sb-Bi-Sn, the concentration of Bi was found to have a strong influence on the corrosion thickness (doubling when Bi content is increased from 20 to 45 at%). In the present study, it is the occurrence of local deeper attacks that increases for higher Bi content in the Sb-Bi binary alloy.

4.3. *Molybdenum*

Mo metal shows good corrosion resistance to Sb-Bi alloys (Figs. 9 and 10). The only effect observed after exposure is a minor interdiffusion of Bi and Mo and an enrichment of the arsenic impurity at the sample surface. It remains unclear whether the interdiffusion is mitigated by the enrichment of As. The As accumulation leads to formation of a distinct As-rich layer in case of Sb_3Bi_7 only. Since As is most probably an impurity of the Sb raw material, the highest amounts of As are expected in the alloy Sb_3Bi_7. Therefore, it is reasonable that in this case the strongest influence of As on the corrosion behavior is found. Even with this influence, the corrosion depth is with 1 μm after 740 h at a very low value.

5. Conclusion

In summary, the results of our work reveal that, among all test specimens, only Mo possesses good corrosion resistance against the liquid Sb-Bi alloys $SbBi_9$, Sb_2Bi_8, and Sb_3Bi_7 at exposure temperatures around 450 °C. The only effect after 740 h exposure is a small interdiffusion of Bi and Mo and an enrichment of As at the Mo surface, which stems from a small impurity of the Sb-Bi alloys. The corrosion behavior of class 316L stainless steels can be regarded as independent of their exact composition. Both the Fe-Cr-Ni steels SS 316L and the Fe-Cr steel T91 show moderate corrosion depths in the range 10–20 μm after 740 h. Locally deeper corrosion attacks (up to 30 μm) are observed mainly after exposure to $SbBi_9$. The corrosion layers are composed of distinct layers with Fe-Cr-Sb and Fe-Sb compounds at the corrosion front and at the sample surface, respectively, which protect the steels from severe dissolution attack. The influence of the arsenic impurity on the corrosion behavior and the susceptibility to local Bi penetration increase as the Sb content of the Sb-Bi alloy decreases. This is explained by a thinner and less stable Fe-Sb layer at the sample surfaces for lower Sb activity in the Sb-Bi alloy. The Fe-Co-Ni alloy Kovar 4J29 shows the strongest corrosion attack among the tested materials. Kovar is locally entirely dissolved and a porous structure of corroded (Ni-depleted) material remains. The depth of this severe corrosion attack is with 800 μm after 740 h largest after exposure to $SbBi_9$. With higher Sb content in the Sb-Bi alloy, a compact Sb-rich phase forms on the sample surface and mitigates the dissolution attack. However, this Sb-rich phase is less effective in mitigating corrosion than the Fe-Cr-Sb compound formed in case of the steels.

CRediT authorship contribution statement

Georg Müller: Funding acquisition, Conceptualization. **Renate Fetzer:** Writing – original draft, Visualization, Investigation. **Annette Heinzel:** Writing – review & editing, Investigation. **Tianru Zhang:** Investigation. **Alfons Weisenburger:** Writing – review & editing, Conceptualization.

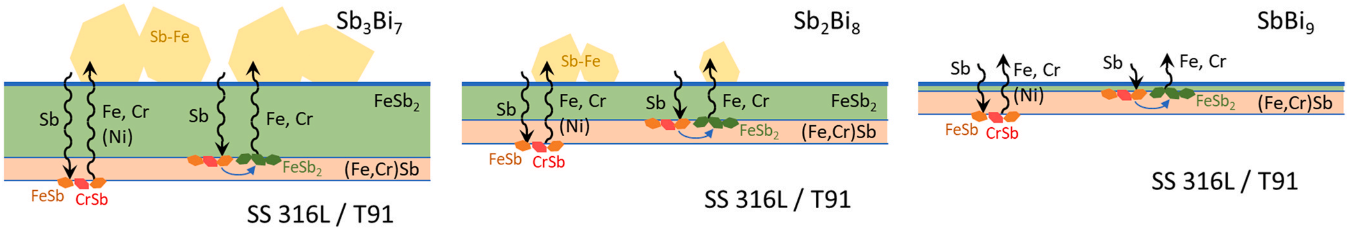

Fig. 11. Proposed corrosion mechanism of steels in liquid Sb-Bi alloys.

Declaration of Competing Interest

The authors declare that they have no known competing financial interests or personal relationships that could have appeared to influence the work reported in this paper.

Data availability

The raw/processed data required to reproduce these findings cannot be shared at this time due to technical or time limitations. The data are available from the corresponding author on reasonable request.

Acknowledgements

The authors are grateful to the Deutsche Forschungsgemeinschaft (DFG) and National Natural Science Foundation of China (NSFC) for funding the DFG-NSFC Sino-German Project (DFG Project Member 411450529): “Study on Corrosion Control and Low-Temperature Electrolytes for Low-Cost Na-based Liquid Metal Batteries”.

References

[1] H. Kim, D.A. Boysen, J.M. Newhouse, B.L. Spatocco, B. Chung, P.J. Burke, D. J. Bradwell, K. Jiang, A.A. Tomaszowska, K. Wang, W. Wei, L.A. Ortiz, S.A. Barriga, S.M. Poizeau, D.R. Sadoway, Liquid metal batteries: past, present, and future, Chem. Rev. 113 (2013) 2075–2099, https://doi.org/10.1021/cr300205k.

[2] K. Wang, K. Jiang, B. Chung, T. Ouchi, P.J. Burke, D.A. Boysen, D.J. Bradwell, H. Kim, U. Muecke, D.R. Sadoway, Lithium-antimony-lead liquid metal battery for grid-level energy storage, Nature 514 (2014) 348–350, https://doi.org/10.1038/nature13700.

[3] S. Zhang, Y. Liu, Q. Fan, C. Zhang, T. Zhou, K. Kalantar-Zadeh, Z. Guo, Liquid metal batteries for future energy storage, Energy Environ. Sci. 14 (2021) 4177–4202, https://doi.org/10.1039/D1EE00531F.

[4] S. Wu, X. Zhang, R. Wang, T. Li, Progress and perspectives of liquid metal batteries, Energy Storage Mater. 57 (2023) 205–227, https://doi.org/10.1016/j.ensm.2023.02.021.

[5] S. Yan, X. Zhou, H. Li, Y. Shen, Y. He, H. Zhou, K. Wang, K. Jiang, Utilizing in situ alloying reaction to achieve the self-healing, high energy density and cost-effective Li||Sb liquid metal battery, J. Power Sources 514 (2021) 230578, https://doi.org/10.1016/j.jpowsour.2021.230578.

[6] H. Li, K. Wang, S. Cheng, K. Jiang, High performance liquid metal battery with environmentally friendly antimony-tin positive electrode, ACS Appl. Mater. Interfaces 8 (2016) 12830–12835, https://doi.org/10.1021/acsami.6b02576.

[7] X. Ning, S. Phadke, B. Chung, H. Yin, P. Burke, D.R. Sadoway, Self-healing Li–Bi liquid metal battery for grid-scale energy storage, J. Power Sources 275 (2015) 370–376, https://doi.org/10.1016/j.jpowsour.2014.10.173.

[8] T. Dai, Y. Zhao, X.H. Ning, R. Lakshmi Narayan, J. Li, Z. wei Shan, Capacity extended bismuth-antimony cathode for high-performance liquid metal battery, J. Power Sources 381 (2018) 38–45, https://doi.org/10.1016/j.jpowsour.2018.01.048.

[9] W. Zhao, P. Li, Z. Liu, D. He, K. Han, H. Zhao, X. Qu, High-performance antimony–bismuth–tin positive electrode for liquid metal battery, Chem. Mater. 30 (2018) 8739–8746, https://doi.org/10.1021/acs.chemmater.8b01869.

[10] K. Cui, F. An, W. Zhao, P. Li, S. Li, C. Liu, X. Qu, Feasibility research of SS304 serving as the positive current collector of Li||Sb-Sn liquid metal batteries, J. Phys. Chem. C. 125 (2021) 237–245, https://doi.org/10.1021/acs.jpcc.0c09629.

[11] W. Liu, H. Yin, K. Du, B. Yang, D. Wang, Corrosion behaviors of iron, chromium, nickel, low-carbon steel, and four types of stainless steels in liquid antimony-tin alloy, Corrosion 77 (2021) 1192–1202, https://doi.org/10.5006/3820.

[12] K. Cui, W. Zhao, D. Zhou, S. Li, C. Liu, P. Li, X. Qu, Stable positive current collectors for Li||Sb–Sn liquid metal batteries, ACS Appl. Energy Mater. 4 (2021) 9013–9021, https://doi.org/10.1021/acsaem.1c01280.

[13] T. Zhang, R. Fetzer, A. Heinzel, A. Weisenburger, C. Tang, M. Stüber, G. Müller, Corrosion behavior of various conductive materials in Sb3Sn7 alloy at 450 °C, Corros. Sci. 227 (2024) 111797, https://doi.org/10.1016/j.corsci.2023.111797.

[14] H. Zhou, H. Li, Q. Gong, S. Yan, X. Zhou, S. Liang, W. Ding, Y. He, K. Jiang, K. Wang, A sodium liquid metal battery based on the multi-cationic electrolyte for grid energy storage, Energy Storage Mater. 50 (2022) 572–579, https://doi.org/10.1016/j.ensm.2022.05.032.

[15] R. Fetzer, T. Zhang, F. Lindner, A. Weisenburger, G. Müller, How cell design affects the performance of sodium-antimony-bismuth liquid metal batteries, J. Power Sources 591 (2024) 233823, https://doi.org/10.1016/j.jpowsour.2023.233823.

[16] L.R. Kelman, W.D. Wilkinson, F.L. Yaggee, Resistance of Materials to Attack by Liquid Metals, Argonne, IL (United States), 1950, https://doi.org/10.2172/4419134.

[17] R.N. Lyon, Liquid-metals handbook, in: in: Superintendent of Documents, U.S. Government Printing Office, Washington 25, D.C., 1952. ⟨https://www.osti.gov/biblio/4377939⟩.

[18] E.L. Reed, Stability of refractories in liquid metals, J. Am. Ceram. Soc. 37 (1954) 146–153, https://doi.org/10.1111/j.1151-2916.1954.tb14013.x.

[19] G. Müller, A. Heinzel, G. Schumacher, A. Weisenburger, Control of oxygen concentration in liquid lead and lead–bismuth, J. Nucl. Mater. 321 (2003) 256–262, https://doi.org/10.1016/S0022-3115(03)00250-2.

[20] W. Timmerhoff, Die Löslichkeit verschiedener Stähle ın Bleischmelzen, Int. J. Mater. Res. 34 (1942) 102–104, https://doi.org/10.1515/ijmr-1942-340503.

[21] T. Ouchi, D.R. Sadoway, Positive current collector for Li||Sb-Pb liquid metal battery, J. Power Sources 357 (2017) 158–163, https://doi.org/10.1016/j.jpowsour.2017.04.104.

[22] K. Cui, P. Li, W. Zhao, C. Liu, S. Li, D. Zhou, X. Qu, Self-healing action of Bi in high-performance Sb–Bi–Sn positive electrodes for liquid metal batteries, J. Power Sources 538 (2022) 231584, https://doi.org/10.1016/j.jpowsour.2022.231584.

[23] G. Coen, J. Van den Bosch, A. Almazouzi, J. Degrieck, Investigation of the effect of lead-bismuth eutectic on the fracture properties of T91 and 316L, J. Nucl. Mater. 398 (2010) 122–128, https://doi.org/10.1016/j.jnucmat.2009.10.021.

[24] A. Heinzel, A. Weisenburger, G. Müller, Corrosion behavior of austenitic steel AISI 316L in liquid tin in the temperature range between 280 and 700 °C, Mater. Corros. 68 (2017) 831–837, https://doi.org/10.1002/maco.201609211.

[25] Y. Xia, Y. Liu, C. Wu, H. Peng, H. Tu, J. Wang, X. Su, 650 and 750 °C isothermal sections of the Cr-Sb-Fe system, J. Phase Equilib. Diffus 39 (2018) 426–436, https://doi.org/10.1007/s11669-018-0653-0.

[26] O. Kidari, P. Chartrand, Thermodynamic evaluation and optimization of the As–Co, As–Fe and As–Fe–S systems, Calphad 82 (2023) 102589, https://doi.org/10.1016/j.calphad.2023.102589.

[27] M. Venkatraman, J.P. Neumann, The As-Cr (arsenic-chromium) system, J. Phase Equilib. 11 (1990) 424–430, https://doi.org/10.1007/BF02898253.